

# Optics Letters

## Optimizing numerical $k$ -sampling for swept-source optical coherence tomography angiography

NAIXING HUANG,<sup>1,2</sup>  TRISTAN T. HORMEL,<sup>1</sup> GUANGRU B. LIANG,<sup>1,2</sup>  XIANG WEI,<sup>1</sup>  YUKUN GUO,<sup>1,2</sup>  SIYU CHEN,<sup>1,2</sup>  AND YALI JIA<sup>1,2,\*</sup> 

<sup>1</sup>Casey Eye Institute, Oregon Health & Science University, Portland, Oregon 97239, USA

<sup>2</sup>Department of Biomedical Engineering, Oregon Health & Science University, Portland, Oregon 97239, USA

\*jjaya@ohsu.edu

Received 11 January 2024; revised 7 February 2024; accepted 9 February 2024; posted 9 February 2024; published 22 February 2024

**High-quality swept-source optical coherence tomography (SS-OCT) requires accurate  $k$ -sampling, which is equally vital for optical coherence tomography angiography (OCTA). Most SS-OCT systems are equipped with hardware-driven  $k$ -sampling. However, this conventional approach raises concerns over system cost, optical alignment, imaging depth, and stability in the clocking circuit. This work introduces an optimized numerical  $k$ -sampling method to replace the additional  $k$ -clock hardware. Using this method, we can realize high axial resolution (4.9- $\mu\text{m}$  full-width-half-maximum, in air) and low roll-off (2.3 dB loss) over a 4-mm imaging depth. The high axial resolution and sensitivity achieved by this simple numerical method can reveal anatomic and microvascular structures with structural OCT and OCTA in both macular and deeper tissues, including the lamina cribrosa, suggesting its usefulness in imaging retinopathy and optic neuropathy.** © 2024 Optica Publishing Group

<https://doi.org/10.1364/OL.518720>

With the ability to provide depth-resolved images of the tissue at resolution approaching the cellular scale, optical coherence tomography (OCT) is useful for retinal imaging. Over the last decade, the development of OCT angiography (OCTA) has extended the features that can be visualized in a single scan from the tissue structure to the vasculature. Given the prevalence of blinding diseases with a vascular component [1,2], OCTA has become an essential imaging modality for ophthalmic practice. However, these advantages must be balanced with some limitations in the conventional OCTA technology: a wide-field scan requires an extended imaging depth to effectively encompass the greater retinal curvature [3]. An extended imaging depth is especially beneficial for identifying pathology in deeper tissues like the lamina cribrosa (LC). An improved ability to image such structures would provide diagnostic and research advantages with optic neuropathy, such as glaucoma [4].

Recently, SS-OCT systems have been used to generate OCTA data because they can provide high sensitivity, extended imaging depth, and scan acquisition speeds [5]. In SS-OCT systems, the OCT signal is obtained by Fast Fourier Transform (FFT) of the interferogram generated from light reflected by a sample and

a reference (a mirror). Interferogram fringes should be linear in wavenumber ( $k$ ) before FFT to realize high axial resolution [6]. However, ensuring linear  $k$ -sampling in SS-OCT systems presents a challenge. Many instruments, including our previous SS-OCT prototypes [5,7], have traditionally relied on an external Mach-Zehnder interferometer (MZI) to achieve this objective. While hardware-driven approaches like MZIs have demonstrated excellent linear  $k$ -sampling, they come hand-in-hand with complexities encompassing cost, optical alignment, and clocking circuit glitches [7,8]. Furthermore, a notable constraint surfaces when the digitizer struggles to clock a high-frequency signal [7,8]. In such cases, the imaging depth must be curbed to avoid spectrum aliasing issues [3]. As an alternative approach, Yasuno *et al.* introduced a numerical  $k$ -sampling method, eliminating the need for a  $k$ -clock or additional hardware. This method has been employed successfully for retinal imaging [9].

In numerical  $k$ -sampling, a primary challenge is phase instability, typically addressed through sweep calibration [17]. Without sweep calibration, the axial resolution may degrade with numerical  $k$ -sampling accuracy, resulting in a reduction in the axial resolution compared to  $k$ -clock methods, often  $\sim 1\ \mu\text{m}$  [10]. This trade-off in axial resolution is reminiscent of the split-spectrum amplitude-decorrelation angiography (SSADA) flow signal generation. SSADA intentionally sacrifices some axial resolution to enhance the OCTA signal sensitivity, eliminate phase instability, and mitigate the impact of bulk eye motion [11]. The loss of axial resolution is deemed acceptable because even at lower axial resolution, the vascular plexuses and complexes can still be isolated, meaning that plexus-specific imaging (one of the major advantages of OCTA imaging) can still be achieved. For the same reason, hypothetically, the numerical  $k$ -sampling method will not reduce the quality of OCT angiograms compared to the phase-stabilized method using hardware.

Therefore, the benefits of using the numerical  $k$ -sampling in wide-field OCTA need to be explored. In this Letter, we propose an algorithm to enhance the  $k$ -sampling accuracy and implement the approach with SSADA to perform real-time, linear-in- $k$  OCT/OCTA retinal imaging on a lab-built SS-OCT system. This showcases the capabilities of our algorithm, enabling high-resolution imaging of retinal vasculature and capillaries in both the macula and the LC without a  $k$ -clock, sweep calibration, MZI, or additional hardware.

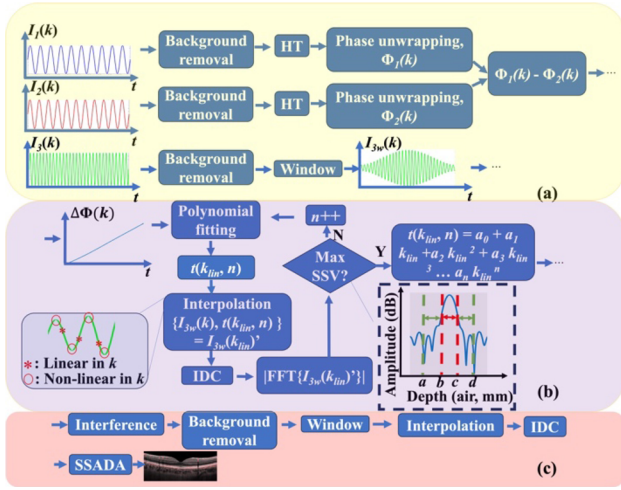


**Fig. 1.** Numerical  $k$ -sampling and OCTA reconstruction. In phase calibration (a), interferogram fringes ( $I_1(k)$ ,  $I_2(k)$ ,  $I_3(k)$ ) from a sample mirror positioned in three different places were measured. Background removal, Hilbert transform (HT), and phase unwrapping were then successively applied to obtain each signal's phase ( $\phi_1(k)$ ,  $\phi_2(k)$ ). Subtraction between the two phases was used to cancel the dispersion.  $I_{3w}(k)$  was obtained after the background removal and a Taylor window. In iterative polynomial fitting (b), the phase shift  $\Delta\phi(k)$  was used to obtain the linear-in- $k$  time interval  $t(k_{lin}, n)$  by linear resampling with the polynomial coefficients, where  $n$  denotes the polynomial fitting order. Iterative dispersion compensation (IDC) and FFT were used to get accurate amplitude information from the interpolated interferogram fringe  $I_{3w}(k_{lin})'$ . Polynomial fitting was iteratively performed by adjusting the order until a maximum sidelobe suppression value (SSV), based on  $I_{3w}(k_{lin})'$ , was obtained (Eq. (1)). To obtain the OCTA signal (c), the optimal  $t(k_{lin}, n)$  from (b) was interpolated from the interferogram fringes. Mean-value background removal, IDC, a Taylor window, and SSADA were applied to produce the angiogram.

The SS-OCT system in this work has been previously reported [5]. It achieved a 4-mm imaging depth with a 1.8-GHz sampling rate using a  $k$ -clock. In this work, a digitizer with a 1.0-GHz sampling rate (Alazar, Inc.), a 200 kHz, 1045-nm central wavelength, a 118-nm tunable range, a short external-cavity swept-source laser (AXSUN, Inc.), and a 470-MHz balanced detector (Thorlabs, Inc.) were used.

Briefly, our OCTA signal generation approach will involve three major steps: phase calibration with a sample mirror at different positions, iterative polynomial fitting, and OCTA reconstruction. The phase calibration extracts the linear-in- $k$  phase information to enable precise interpolation. The iterative polynomial fitting produces the optimal linear-in- $k$  time interval  $t(k_{lin}, n)$ , where  $n$  denotes the order of the polynomial fit. This process minimizes the phase noise error. The OCTA reconstruction based on the optimal  $t(k_{lin}, n)$  can then acquire the high-resolution OCT/OCTA signal.

The first step, phase calibration (Fig. 1(a)), begins with the acquisition of interferogram fringes using a sample mirror located 1 mm ( $I_1(k)$ ), 1.1 mm ( $I_2(k)$ ), and 4 mm ( $I_3(k)$ ) from the zero-path delay. The  $I_1(k)$  and  $I_2(k)$  were placed at 1 and 1.1 mm, respectively, near the zero-path delay for robust phase unwrapping but cannot overlap the DC and AC artifacts, and then the DC and AC were removed by a digital filter. The phase calibration can be improved by removing the interferogram background; we

measured this background by successively blocking the sample arm, the reference arm, or both, and then summing the resulting interferograms as the total background [8]. Following the background suppression, a Hilbert transform was applied to retrieve the instantaneous phase information. We then applied phase unwrapping to the result. Additionally, the second-order dispersion should be canceled by subtracting the dispersion phase, which can otherwise degrade the accuracy of the calibration process [8,9]. The resulting non-linear phase shift  $\Delta\phi(k)$  was interpolated by a spline interpolation function, mitigating the phase noise from the phase unwrapping. The  $I_{3w}(k)$ , obtained by applying background removal and the Tyler window function to  $I_3(k)$ , was used as a global reference over the 4-mm imaging range in the iterative polynomial fitting (Fig. 1(b)), assuming no depth-dependent dispersion over the 4-mm imaging depth.  $\Delta\phi(k)$  and  $I_{3w}(k)$  were employed to determine the resampling positions for subsequent steps (Fig. 1(b)).

The second step is the iterative polynomial fitting (Fig. 1(b)). The original time interval  $t$  was linearly resampled into the  $t(k_{lin}, n)$  with the polynomial coefficients. Nevertheless,  $\Delta\phi(k)$  is susceptible to phase noise due to phase unwrapping imperfections that can cause inaccurate  $t(k_{lin}, n)$  [12]. Utilizing an imprecise  $t(k_{lin}, n)$  during the interpolation not only compromises axial resolution but also intensifies sidelobes (the unwanted peaks surrounding the maximum). These issues can primarily be attributed to the non-linearity in  $k$ . Window functions and iterative dispersion compensation (IDC) can suppress sidelobes and resolution degradation but hinge on the accurate interpolation of  $t(k_{lin}, n)$  since they rely on the source spectrum as a function of  $k$  [6,13]. To compensate for this effect, we propose using sidelobe suppression based on  $I_{3w}(k_{lin})'$  as an indicator to evaluate the accuracy of  $t(k_{lin}, n)$ . The sidelobe suppression value (SSV, in dB) is determined by the mean value of the sidelobe region (a to b and c to d, Fig. 1(b)) around the FWHM (b to c, Fig. 1(b)). SSV is defined as

$$\text{SSV} = 20\log_{10} \left[ \frac{\sum_b^c A(x)\Delta x}{N_{bc}} - \left( \frac{\sum_a^b A(x)\Delta x}{N_{ab}} + \frac{\sum_c^d A(x)\Delta x}{N_{cd}} \right) \right], \quad (1)$$

where  $A$  denotes the amplitude of  $I_{3w}(k_{lin})'$  and  $x$  denotes depth.  $N_{bc}$ ,  $N_{ab}$ , and  $N_{cd}$  indicate the number of pixels within specific depth ranges. In this work the  $N_{ab}$  and  $N_{cd}$  are 20 pixels.

We chose an initial polynomial order of  $n_0 = 3$  to generate the  $t(k_{lin}, n)$ . IDC was applied to address the residual dispersion. The amplitude  $A(x)$  of the  $I_{3w}(k_{lin})'$  was obtained by FFT to calculate the SSV. The SSV was recorded iteratively with increasing order until a maximum was reached (Fig. 2(b)); thus, the optimal  $t(k_{lin}, n)$  was obtained.

The third step is the OCTA reconstruction (Fig. 1(c)). The system performed real-time linear-in- $k$  retinal imaging by interpolating the optimal  $t(k_{lin}, n)$  from Fig. 1(b). Here, the mean value of all interferogram fringes (a.u.) was subtracted from each individual fringe in order to remove the background. A Taylor window was applied for spectral reshaping and sidelobe suppression [7], and spline interpolation with a GPU (graphic processing unit)-accelerated CUDA function was performed. IDC was used to optimize the dispersion in the eye during retinal imaging [13]. SSADA with four split windows generated the OCTA data.

In the post-processing, cross correlation was used to adjust trigger jittering and the axial eye movement [5]. *En face* OCT images were projected with mean-value projection, whereas *en*

**Table 1. Scanning Protocols**

FOV	A-Scan Sampling Density	B-Scan Repeats	Motion Tracking	Acquisition Time(s)
3 × 3 mm	616 × 616	3	No	3.87
6 × 6 mm	848 × 848	3	Yes	6.16
10 × 10 mm	1024 × 1024	3	Yes	12.35

*face* OCTA images were projected with maximum projection. OCTA projection artifacts in the deep capillary complex were removed by subtracting the superficial vascular complex flow signal [14]. Layer segmentation was done with the COOL-ART software [4]. The lamina cribrosa's boundary is defined between the prelamina and retrolamina according to a previous study [15].

We sampled volunteer retinas at 2560 points per A-scan. The sampling density varied in the number of A-scans and B-scans accommodating different fields of view (FOV; Table 1). We employed a raster scan pattern throughout. To effectively counteract a potential eye motion, motion tracking was activated specifically for the larger FOV scans, ensuring the image quality and stability [16]. The system's sensitivity was measured at 1.1 mm from the zero-path delay using a neutral density filter (ND = 2.0) and a silver mirror [5].

With our optical configuration, the lateral optical resolution of our system is 19  $\mu\text{m}$ . The incident power on the cornea is 2.0 mW, which is within the ANSI Z136.1-2014 standards for 1060-nm light. The maximum sensitivity was measured at 102.2 dB, with 2.3-dB roll-off measured at 4 mm from the zero-delay (Fig. 2(a)). In the pursuit of accuracy, we found that not all fitting orders ( $n$ ) contribute to the enhancement of SSV. Through iterative polynomial fitting, we determined that the maximum improvement in SSV occurs when  $n = 8$ , which yields an average SSV of 24.1 dB. (Figure 2(b)). Utilizing the iterative polynomial fitting, we successfully automated the acquisition of the optimal

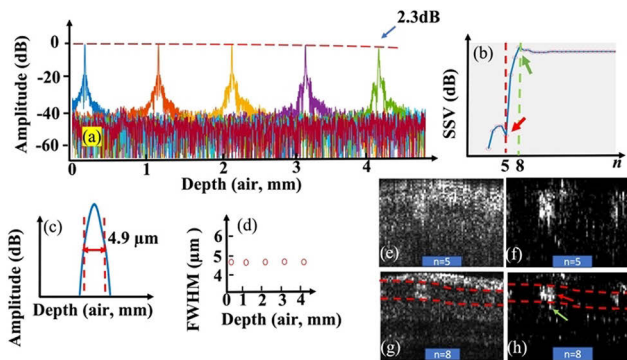


**Fig. 2.** SS-OCT performance. (a) Color-coded traces showing signal amplitude at different depths. The overall signal roll-off is 2.3 dB over a 4-mm imaging depth. (b) Sidelobe suppression value (SSV; Eq. (1)) is non-monotonic in polynomial fitting order  $n$ . (c) Point spread function of our system measured at 1.1 mm from the zero-path delay. The full-width-half-maximum (FWHM) annotated by a red double arrow showing 4.9  $\mu\text{m}$  of the axial resolution. (d) FWHM of our system measured over the entire imaging depth range. (e)–(h) Four cross-sectional B-scans extracted from the same 10 × 10-mm scan showing the comparison between different polynomial fitting orders ( $n = 5$  or 8). (e) and (f) OCT (left) and OCTA (right) images with inaccurate interpolation, (g) and (h) optimal OCT (left) and OCTA (right) images using our method.

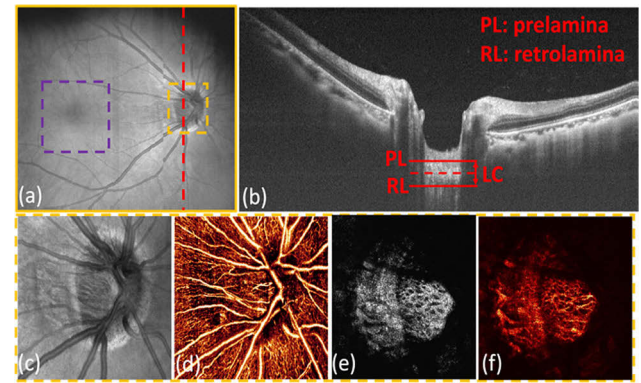


**Fig. 3.** OCT and OCTA of the peripapillary region. (a) *En face* OCT (10 × 10 mm). (b) B-scan crossing over the disk at the location of the red dashed line in (a). (c) and (d) *En face* structural OCT (c) and OCTA (d) of the disk area (3 × 3 mm). (e) and (f) Structural OCT and OCTA C-scan of the lamina cribrosa (LC) at the depth indicated by the red dashed line in (b). The dashed purple box in (a) shows the field of view captured in Fig. 4 below.

$t(k_{lin}, n)$ . The point spread function of our system, as measured in the dB scale at 1.1 mm from the zero-path delay, yielded a maximum axial resolution of 4.9  $\mu\text{m}$  in air (Fig. 2(c)). Measured resolutions over the 4-mm imaging range showed an acceptable deviation ( $\sim 0.8 \mu\text{m}$ ) from the theoretical resolution of 4.1  $\mu\text{m}$  (Fig. 2(d)). The optimal interpolation with  $n = 8$  significantly improved the OCT quality, as shown by the clear boundary of the ganglion cell layer (segmented by the red dashed curves) (Figs. 2(e) and 2(g)). The angiogram of the vascular (red arrow, Fig. 2(h)) and complex (green arrow, Fig. 2(h)) showed a clear isolation with the optimization.

We examined healthy adult volunteers using our SS-OCT system, employing three sequential scan patterns as outlined in Table 1. We initiated a wide-field 10 × 10-mm scan to provide a preview of the retina (Fig. 3). Notably, motion tracking was essential for reducing eye motion (Fig. 3(a)). In cross-sectional images the imaging depth achieved by this system can effectively reveal the lamina cribrosa (LC). Leveraging the high imaging depth and sensitivity provided by our approach, the improved resolution and contrast were demonstrated in delineating the LC's boundary. Moving forward, we adopted the second scan pattern, featuring a 3 × 3-mm field of view, to acquire more detailed information regarding the disk area of interest, highlighted within the orange dashed box in Fig. 3(a). The axial positioning of the cross-sectional LC C-scans (Figs. 3(e) and 3(f)) was centered between the prelaminar and retrolaminar regions. This position unveiled the porous structure of the deep LC region (Fig. 3(e)) with the corresponding OCTA capillary network within the LC (Fig. 3(f)).

The third scan (6 × 6 mm) was executed in the macular region (purple box in Fig. 3(a)). Our approach delivered OCT cross-sectional images characterized by visible layer boundaries (Figs. 4(a) and 4(b)). The distribution of nerve fibers and capillaries was evident, resulting from our system's lateral resolution (Figs. 4(c)–4(e)). Furthermore, we presented *en face* OCTA images that depict the vascular and capillary scale information. Notably, the foveal avascular zone exhibited a well-defined boundary without any visible background (Figs. 4(f)–4(h)).

In this Letter, through the iterative refinement of polynomial fitting guided by the SSV indicator, we achieved an optimal



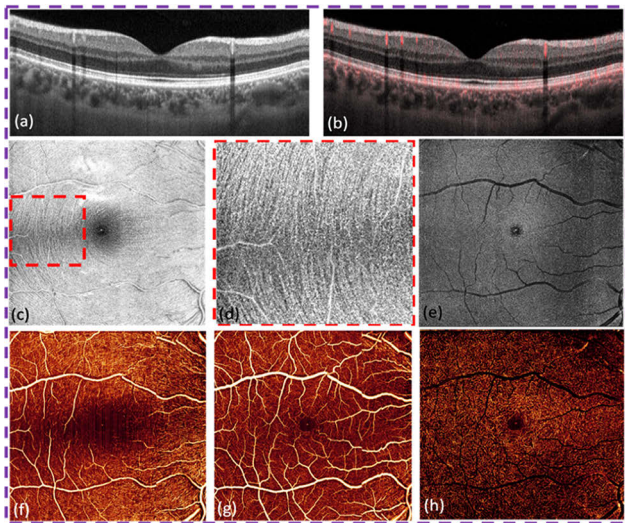


**Fig. 4.** Structural OCT and OCTA ( $6 \times 6$  mm) of the macular region. (a) Cross-sectional OCT crossing over the center of the fovea. (b) Same image with the flow signal overlaid in red. (c) *En face* structural OCT of the nerve fiber layer and (d) magnified image showing individual nerve fiber bundles. (e) *En face* OCT of the deep capillary plexus, (f)–(h) *En face* OCTA of the nerve fiber layer plexus, ganglion cell layer plexus, and deep capillary complex.

linear-in- $k$  time interval  $t(k_{lin}, n)$ , culminating in improved sensitivity and resolution (Fig. 2), which generated plexus-specific OCTA images of the macular region and the angiogram of the deep LC as a novel feature to previous numerical and  $k$ -clock methods [5,9].

Note that our approach simplified the SS-OCT image acquisition by eliminating the need for expensive components like  $k$ -clocks, high-speed digitizers, phase stabilization techniques, and MZIs, which opens the door for affordable digitizer options with varying sampling rates, making wide-field, megahertz SS-OCT systems more feasible outside research systems.

In future work we will validate and improve our method with different lasers and dispersion, ensuring continuous system refinement to benefit the research and clinic in retinal diseases and optic retinopathies.

**Funding.** National Institutes of Health (P30 EY010572, R01 EY023285, R01 EY024544, R01 EY027833, R01 EY031394, R01 EY035410, T32 EY023211, UL1TR002369); the Jennie P. Weeks Endowed Fund; the Malcolm M. Marquis, MD Endowed Fund for Innovation; Unrestricted Departmental Funding Grant and Dr. H. James and Carole Free Catalyst Award from Research to Prevent Blindness (New York, NY); Edward N. & Della L. Thome Memorial Foundation Award, and the Bright Focus Foundation (G2020168, M20230081).

**Acknowledgment.** This work was supported by the National Institute of Health (R01 EY035410, R01 EY027833, R01 EY024544, R01 EY031394, R01 EY023285, T32 EY023211, UL1TR002369, P30 EY010572); the Jennie P. Weeks Endowed Fund, the Malcolm M. Marquis, MD Endowed Fund for Innovation; an Unrestricted Departmental Funding Grant and Dr. H. James and Carole Free Catalyst Award from Research to Prevent Blindness (New York, NY); Edward N. & Della L. Thome Memorial Foundation Award, and the Bright Focus Foundation (G2020168, M20230081).

**Disclosures.** Yali Jia: Optovue/Visionix, Inc. (P, R), Optos (P), Genentech, Inc (P, F). These potential conflicts of interest have been reviewed and managed by OHSU. Other authors declare no conflicts of interest related to this article.

**Data availability.** Data underlying the results presented in this paper are not publicly available at this time but may be obtained from the authors upon reasonable request.

## REFERENCES

1. Z. L. Teo, Y.-C. Tham, M. Yu, *et al.*, *Ophthalmology* **128**, 1580 (2021).
2. P. Song, Y. Xu, M. Zha, *et al.*, *J. Global Health* **9**, 010427 (2019).
3. S. Ni, T.-T. P. Nguyen, R. Ng, *et al.*, *Opt. Lett.* **46**, 5878 (2021).
4. Y. Jia, J. M. Simonett, J. Wang, *et al.*, *Invest. Ophthalmol. Visual Sci.* **58**, 5188 (2017).
5. X. Wei, T. T. Hormel, Y. Guo, *et al.*, *Biomed. Opt. Express* **10**, 6286 (2019).
6. M. Wojtkowski, R. Leitgeb, A. Kowalczyk, *et al.*, *J. Biomed. Opt.* **7**, 457 (2002).
7. S. Chen, B. Potsaid, Y. Li, *et al.*, *Sci. Rep.* **12**, 992 (2022).
8. X. Attenu, R. M. Ruis, C. Boudoux, *et al.*, *J. Biomed. Opt.* **24**, 1 (2019).
9. Y. Yasuno, Y. Hong, S. Makita, *et al.*, *Opt. Express* **15**, 6121 (2007).
10. B. Potsaid, B. Baumann, D. Huang, *et al.*, *Opt. Express* **18**, 20029 (2010).
11. Y. Jia, O. Tan, J. Tokayer, *et al.*, *Opt. Express* **20**, 4710 (2012).
12. B. Dong, N. Huang, Y. Bai, *et al.*, *Opt. Lett.* **46**, 5914 (2021).
13. M. Wojtkowski, V. J. Srinivasan, T. H. Ko, *et al.*, *Opt. Express* **12**, 2404 (2004).
14. T. T. Hormel, D. Huang, and Y. Jia, *Quant. Imaging Med. Surg.* **11**, 1120 (2020).
15. S. C. Park and R. Ritch, *Saudi J. Ophthalmol.* **25**, 363 (2011).
16. X. Wei, T. T. Hormel, Y. Guo, *et al.*, *Biomed. Opt. Express* **11**, 3234 (2020).
17. M. J. Ju, M. Heisler, A. Athwal, *et al.*, *Biomed. Opt. Express* **9**, 2336 (2018).